1st Latin-American Workshop on Structural Health Monitoring
LATAM-SHM 2023
December, 5-8 2023

A STRUCTURED LIGHT SYSTEM FOR MONITORING METALLIC POWDER BED ADDITIVE MANUFACTURING

MICHAEL D. TODD[*], NIALL O'DOWD[+,*] AND ADAM WACHTOR[†]

[*] Department of Structural Engineering, University of California San Diego, 9500 Gilman Drive 0085, La Jolla, California 92093-0085 USA
email: mdtodd@ucsd.edu

[+] Phase-3D, Chicago, Illinois 69608 USA
Email: niall@phase-3.com, http://additivemonitoring.com

[†] Los Alamos National Laboratory, Los Alamos, New Mexico 87545 USA
email: ajw@lanl.gov

Key words: metallic additive manufacturing, structured light, uncertainty quantification

Abstract. Powder bed-based metallic additive manufacturing (MAM) processes are rapidly maturing and being adopted in numerous industrial sectors ranging from aerospace to energy to transportation. Build processes and control of those processes are both still in an evolving state, leading to variable part quality. Part quality control has emerged as one of the big challenges, since most fabrication processes require meeting quality assurance protocols. This paper describes a structured light system using a low-cost camera and projector that exploits digital fringe projection to achieve surface profiling of MAM parts. The novelty in this approach lies in a measurement model that propagates uncertainty in captured pixel images (whether due to shot noise or frame-to-frame other sources of variability) to converted phase noise and ultimately to surface profile uncertainty. Another advantage of the model is that the surface profile is given in absolute physical units, as opposed to unreferenced units or relative measurements. Fundamental Gaussian pixel noise is propagated nonlinearly through phase conversion and surface profile estimation to yield a posterior probability density function of the surface profile; this posterior probability density is analytically tractable and supports a very generalized correlation model in the noise both in time and space. Such as posterior enables the measurement process to provide the probabilistic support required for MAM part quality control decisions. Results from a prototype system on MAM parts are demonstrated, including validation of the measurement model, on manufactured surface defects in a powder bed MAM build. (Approved for release LA-UR-23-31857)

1 INTRODUCTION

Additive manufacturing (AM), otherwise known as industrial 3-dimensional (3-D) printing, is a manufacturing technique characterized by repeatedly adding material in a layering way to create the target structure [1]. The typical AM process begins with a computer-aided design

(CAD) file which is then converted to a tool path, then actuated by the AM machine (often referred to as 3-D printer). Many distinct methods of AM have been invented and utilized per their individual strengths and weaknesses, though there are several features which are common among most methods, such as high designed freedom, high speed, low cost for small batches, and low investment cost. Although the earliest AM processes can be traced to stereolithography with polymers in the late 1980s, the advent of the first recognized metal AM system occurred in 1994 by EOS, dubbed the EOSINT M250, which operated via direct metal laser sintering (DMLS) [2], also known as powder bed fusion (PBF); this is currently the dominant AM technology used in the modern aerospace industry. Most PBF techniques utilize a similar manufacturing process, by first raking metallic powder over a flat build plate within a pressurized inert gas build chamber. Then, one or more welding beams or lasers melt or sinter the powder in the pre-designated pattern calculated from the CAD part file. The build chamber lowers, and a new layer of metal powder is raked across the newly formed solid layer and surrounding unfused powder. This process repeats for each layer of the part.

Substantial time and resources are spent after the MAM build process for final part preparation and certification. Post processing includes support structure removal, hot isostatic pressing, surface finishing, chemical treatments. Traditional quality control (QC) approaches including ultrasound, thermography, penetrant testing, eddy current, and x-ray computed tomography provide either localized or whole-part quality assessment after the part is already fully constructed, resulting in wasted fabrication time and materials if the part does not pass inspection. More importantly, the access of these inspection techniques is limited to the external faces of the manufactured part, making the quality of the internal features unknown, which may have been the driving reason for the part to be produced by MAM.

A main source of final-build defects in PBF are powder-based defects (PBDs). These defects include striations, depressions, and clumping, and can lead to detrimental part defects such as keyhole porosity formation, lack-of-fusion (LoF), and even damage to the recoater blade [3-6]. A common denominator among these PBD defects is their localized height expression in the powder layer. Digital fringe projection (DFP) [7] is a technique that uses the visible spectrum to diagnose PBDs, through measurement of the exposed powder layer and fused layer. DFP is a type of structured light sensing that uses varying light intensity patterns, e.g., fringes, projected onto the part or unfused powder and a camera which captures the deformation of the incident fringes. By projecting a series of predefined patterns, a 3D model of the part's surface may be created with real-world dimensional units. The speed of this technique is limited mostly by post-processing; data acquisition time can be reduced below 3 seconds if the projector and camera frames are synchronized. The short data acquisition time make DFP suitable for potential implementation in closed feedback-loop control. This work prototypes a low-cost DFP system designed for surface profiling in a MAM production application. The primary novelty lies in the additional development of a complete measurement model with uncertainty quantified, resulting in confidence intervals on height estimations at each pixel. Such a design could support MAM part accept/reject decision-making or production feedback control in accordance with standardized industrial practices.

2 DIGITAL FRINGE PROJECTION MEASUREMENT MODEL

A general schematic of a DFP process is shown in Figure 1 (left), with a photograph of the

prototype on the right.

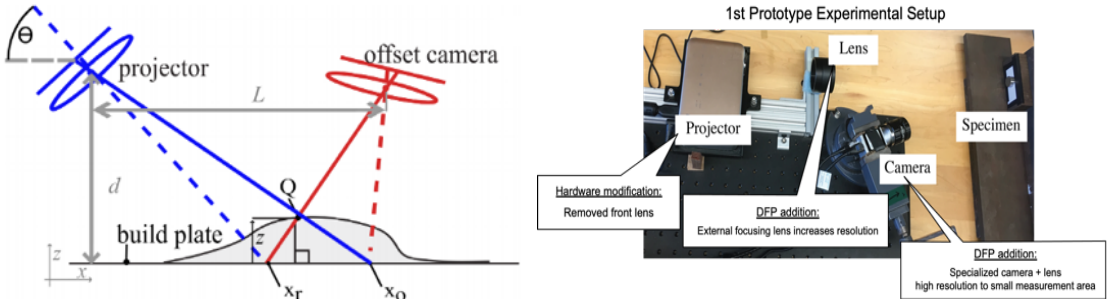

Figure 1. General schematic of DFP process (left), and physical prototype (right).

The DFP process begins with an optical phase measurement obtained by projecting a series of patterns on to a scene and recording the resulting distortion of the patterns caused by the measured object. The distortions are interpreted through *differential* phase measurement; a series of fringe patterns are first projected onto a flat reference plane, denoted by the subscript r in Figure 1), and then placing the object under test (denoted by the subscript o in Figure 1) into the scene, which deforms the incident projected fringe pattern. For any point of interest Q, the camera records images of sinuoidal fringes on both surfaces, where the measured pixel intensity $I_{(r,o)}$ on either measurement surface (r or o) at any given location $x_{(r,o)}$ is given by

$$I_{(r,o)} = A_{(r,o)} + B_{(r,o)} \cos\left(2\pi x_{(r,o)} / P\right) = A_{(r,o)} + B_{(r,o)} \cos\left(\phi_{(r,o)} + \phi_c\right), \tag{1}$$

where P is the fringe pitch, $A_{(r,o)}$ and $B_{(r,o)}$ are the ambient light intensity and the projected fringe contrast at $x_{(r,o)}$, and ϕ_c is the carrier phase offset accounting for the spatial phase difference of the measurement point in relation to the projected fringe pattern. Using similar triangle geometry, the object height z in physical units at interest point Q is given by the the difference between measured reference and object phases

$$z = \frac{d\left(x_o - x_r\right)}{L + x_o - x_r} = \frac{Pd\left(\phi_o - \phi_r\right)}{2\pi L + P\left(\phi_o - \phi_r\right)}. \tag{2}$$

The nonlinear encoding of the phases $\phi_{(r,o)}$ in Equation (1) requires a demodulation approach to recover them. This is accomplished by projecting N phase-shifted images on to both reference and object scenes with equipartitioned spatial shifts $\delta_k = 2\pi k/N$, $k = 1...N$ (sometimes referred to as "bins"). The intensity in each bin may then be given by

$$I_{(r,o),k} = A_{(r,o)} + B_{(r,o)} \cos\left(\phi_{(r,o)} + 2\pi k / N + \phi_c\right). \tag{3}$$

By appropriate summing over the phase-shifted intensities, the reference and object phases at the point of interest may be recovered, assuming nonlinear projector gamma issues are neglible, by

$$\phi_{(r,o)} = -\tan^{-1}\left(\frac{\sum_{k=1}^{N} I_{(r,o),k}\sin\delta_k}{\sum_{k=1}^{N} I_{(r,o),k}\cos\delta_k}\right). \tag{4}$$

The measured ideal intensities are, in practice, corrupted by pixel noise, which may be modeled by an additive term $\varepsilon_{(r,o),k}$ in Equation (3). These noise-corrupted intensities may then be substituted into Equation (4) to get the measured object and reference phases, which are then subtracted as shown in Equation (2) to get the height estimate z. The phase noise κ may be defined as the difference between this noisy differential measurement and the idealized differential measurement, and it may be shown that

$$\kappa = \tan^{-1}\left(\frac{\sum_{k=1}^{N}\sin\left(2\pi k/N+\phi_c\right)\bar{\varepsilon}_{r,k} - \sin\left(2\pi k/N+\phi_c+\phi_o-\phi_r\right)\bar{\varepsilon}_{o,k}}{1+\sum_{k=1}^{N}\cos\left(2\pi k/N+\phi_c\right)\bar{\varepsilon}_{r,k} + \cos\left(2\pi k/N+\phi_c+\phi_o-\phi_r\right)\bar{\varepsilon}_{o,k}}\right), \tag{5}$$

where the overbars on the noise terms indicate normalization of the noise by the fringe contrasts $B_{(r,o)}$, and quadratic terms inside the numerator and denominator of Equation (5) are ignored. This equation may be interpreted as a noise transfer function, where pixel noise structure $\varepsilon_{(o,r),i}$ in the measured intensities gets converted to observed phase noise κ in the output. As expected, when $\bar{\varepsilon}=0$, $\kappa=0$.

This phase noise propagates into the surface height estimation in Equation (2); if the height estimation error χ is defined—similar to the way the phase noise was defined—as the difference between the noisy height estimation and ideal height estimation, then it may be shown that

$$\chi = \frac{\kappa P(d-z)^2}{2\pi dL + \kappa P(d-z)}. \tag{6}$$

where κ is given by Equation (5), resulting in a complete noise transfer function from pixel intensity noise to surface height noise. Using change of variables formula, the probability density of χ may be found as

$$p(\chi) = \frac{p(\kappa)}{\left|\partial\chi/\partial\kappa\right|} = \frac{2\pi dL}{P(\chi+z-d)^2}p(\kappa), \tag{7}$$

where $p(\kappa)$ is the probability density function of the phase noise, which would be derived from Equation (5) under some assumption or model for the pixel intensity noise, $p(\bar{\varepsilon})$. Using a generalized Gaussian noise structure for $\bar{\varepsilon}$, which is a very common observation with pixel noise, the corresponding phase density $p(\kappa)$ was derived in [8], followed by the corresponding derivation of $p(\chi)$ in [9]. The final expression for $p(\chi)$ is too complex to reproduce here, and the interested reader is referred to the references [8] and [9].

2 APPLICATION TO POWDER BED EXPERIMENT

This section presents a parametric study of evaluating multiple measurement parameters, employing the uncertainty models developed, in assessing PBDs with the proposed DFP monitoring system. The effects of varying illumination angle θ, number of projections N, and fringe pitch P are explored to determine optimal testing parameters for in-situ PBD monitoring.

Manufactured PBDs were created using a modified recoater blade with four damage locations representative of the size and shape that typically occur in the PBF process. The "pristine" recoater blade was used to create a uniform powder bed to serve as the reference surface, and the "defective" recoater blade was used to create realizations of raised-streak PBDs. The "defective" blade was fabricated with a set of four notches, increasing in size and width, and this was used to create PBD realizations. Each realization of PBDs were made using the same raking motion to move powder across the aluminum tray, producing an intrinsically random, but consistent surface structure (Figure 2(left)). Four streak PBDs, of approximate heights of 150−180 μm, 105−120 μm, 45−75 μm, and 20−45 μm for PBDs 1-4 shown in Figure 2(right). A Keyence VHX-1000 height measurement microscope was used to characterize the PVDs as "ground truth." Pixel density in this study were approximately 50μm. The output triggering functionality of the projector was used to trigger camera image acquisition. This allowed the capture of fringe images at uniform intervals to eliminate projector "draw lines" which occur without synchronization. Full calibration and experimental details are given in [10].

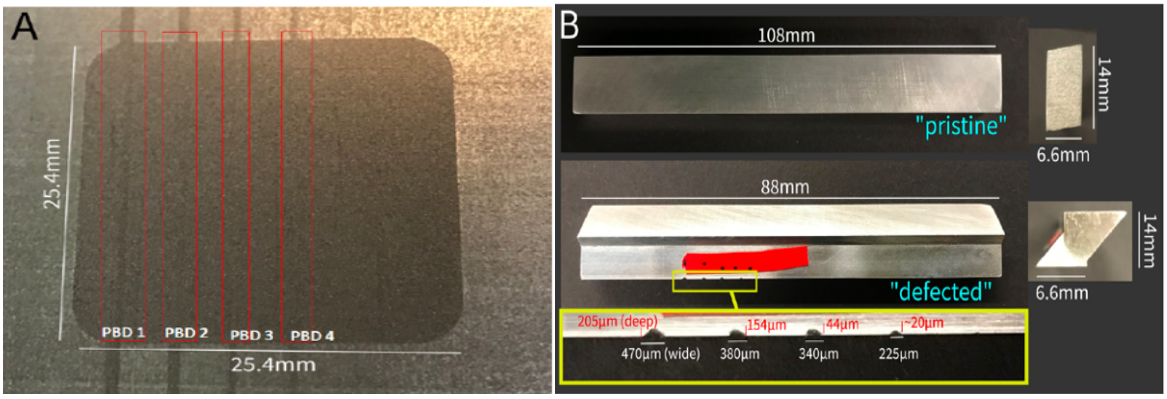

Figure 2. General schematic of DFP (left), and physical prototype implementation (right).

To estimate the effects of the uncertainty field on DFP measurements, the mean and standard deviation were computed from $p(\chi)$. With these expressions, the ideal differential height single-point standard deviation was calculated for the average level of pixel intensity noise and used to determine the fringe P selected for each experimental setup. For reference, the experimental fringe contrast was approximately 90 units of pixel intensity; with an average standard deviation of 1.67 pixel intensity units, that equates to an average of .0186 pixel noise normalized by fringe contrast. Significantly higher fringe contrast was achieved for illumination angles $\theta > 25^{\circ}$, but for the sake of consistency, a contrast value achievable by all measurement angles was selected.

Figure 3 shows the selected parameters for experiment for all four illumination angles θ, all four fringe pitches P, and all five fringe projection bin numbers N. The green shaded areas correspond to DFP resultant height noise approximately 1/2 of the measured height of each

PBD streak, which could be argued is the minimum sensitivity required to detect a single pixel-sized PBD with 95% confidence. The colored series lines show how the ideal standard deviation of measurement increases for increasing fringe pitch P, for a range of bin numbers N. The gray dashed lines show the selected P for each angle; each four representing similar resultant calibration constants.

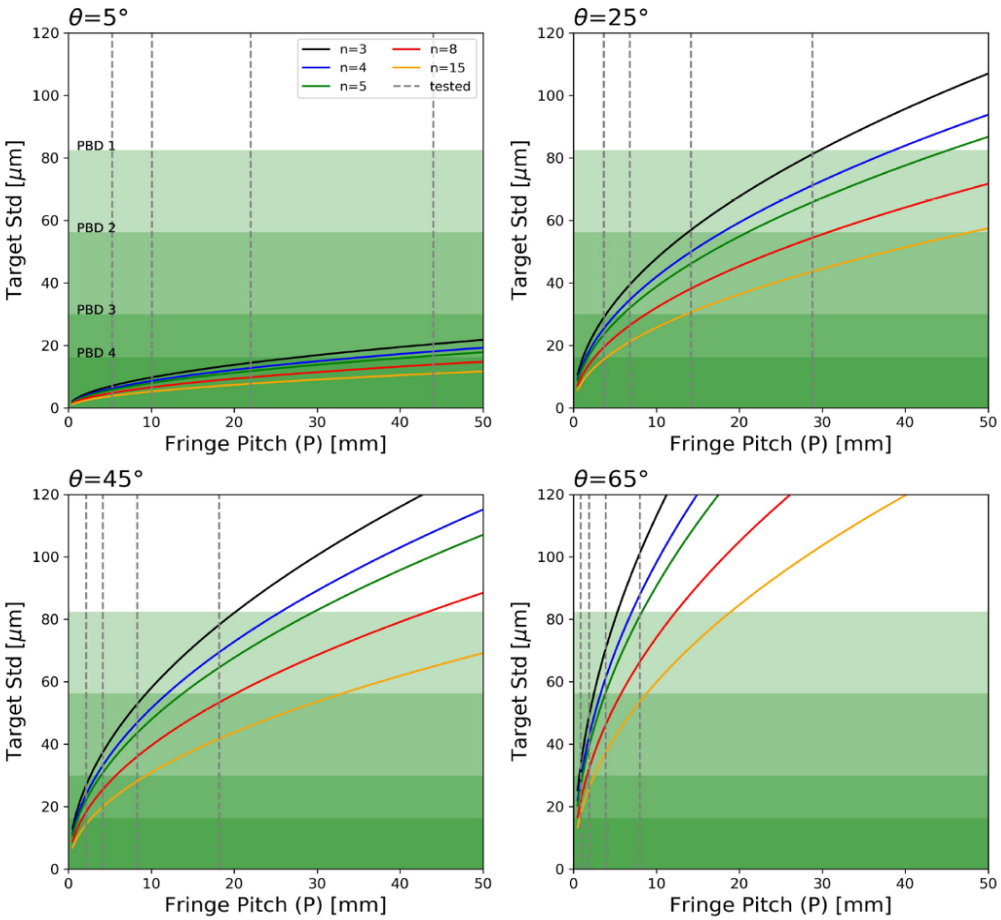

Figure 3. Parameter selections for the experiment with varying projection count N, pitch P, and illumination angle θ. The green shaded areas show the regions of minimum required noise to resolve PBDs with heights characteristic of experiment.

To summarize the findings across all the combinations of tested parameters, the noise distributions of ensemble experimental differential height measurements were compared to the estimated single-point uncertainty from theory. Figure 4 shows the estimated and experimental average noise fields on differential height measurements across the parameters θ,N,P. Estimated differential height measurement noise is shown with filled circles and solid bars representing a single standard deviation, and the experimental full field noise median is shown with X's and error bar caps representing a single standard deviation. The green areas in the figure correspond to minimum levels of differential height noise required to detect the corresponding PBD, at a 95% confidence interval for a single measurement point.

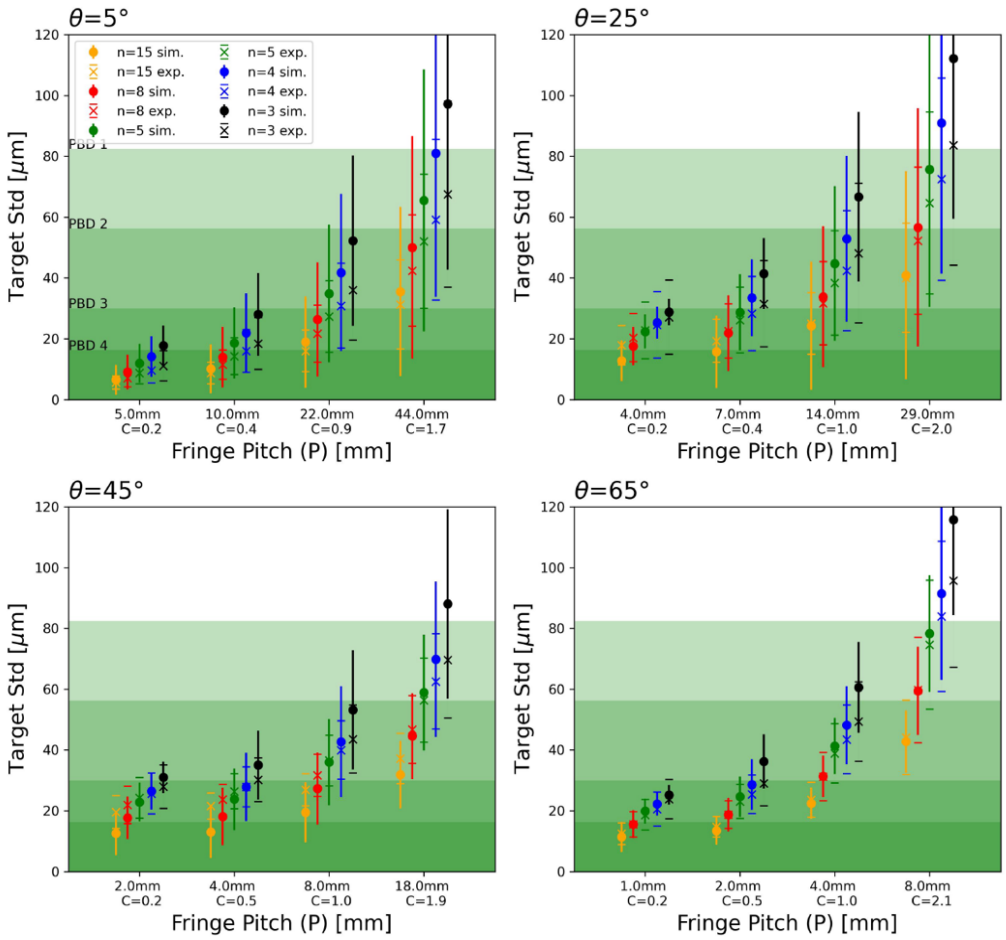

Figure 4. Measured differential height noise across iterations for a range of illumination angles θ, bin number N, fringe pitch P. Green areas show the minimum experimental value of uncertainty required to detect a single pixel of the corresponding PBD at 95% (or 2σ) confidence. Experimental points are shown with error bars of a single standard deviation. Uncertainty model estimations are shown with filled circle markers.

The uncertainty model summarized the average observed noise levels of the experiments, with agreement for each parameter combination within a single standard deviation. For measurement parameters across all θ, for $N > 5$ and calibration constant $C < 1.7$, the measurement model estimated the experiment very accurately. When P is increased (for equivalently $C > 1$), the model begins to erroneously overestimate the measurement noise, which becomes large enough to impact the most severe PBD streaks. A higher discrepancy between the model estimations and the experimental noise for $N < 5$ was also observed expectedly, as low N inadequately represents the assumed sinusoidal spatial bin diversity.

To showcase an example of the model's estimation of differential height uncertainty, a representative case comparing observed differential height noise across all 15 iterations and estimated uncertainty is presented in Figure 5. Figure 5 (upper left) shows the measured standard deviation of differential height measurements across all iterations, for an example measurement with $N = 5$, $\theta = 45°$, and $P \approx 17$mm. Figure 5 (upper right) shows the estimated standard deviation of the PDF produced by the single point uncertainty model for the same

measurement parameters. Figure 5 (lower) shows the distribution of the differential height measurements and the estimated uncertainty distribution of sample points 1 and 2 from the upper sub-figures. Observed in the upper left portion Fig. 5, differential height measurement noise was non-uniform across the field of measurement and varied dramatically depending on subtle surface textures. The uncertainty model captured these noise structures, seen in the upper right sub-figure of Fig. 5, allowing for pixel-by-pixel statistical confidence to determine the probability of each height point. The distributions of differential height noise and estimated uncertainty of example pixels 1 and 2 is shown in the lower sub-figure of Fig. 5, showcasing excellent agreement between model and simulation.

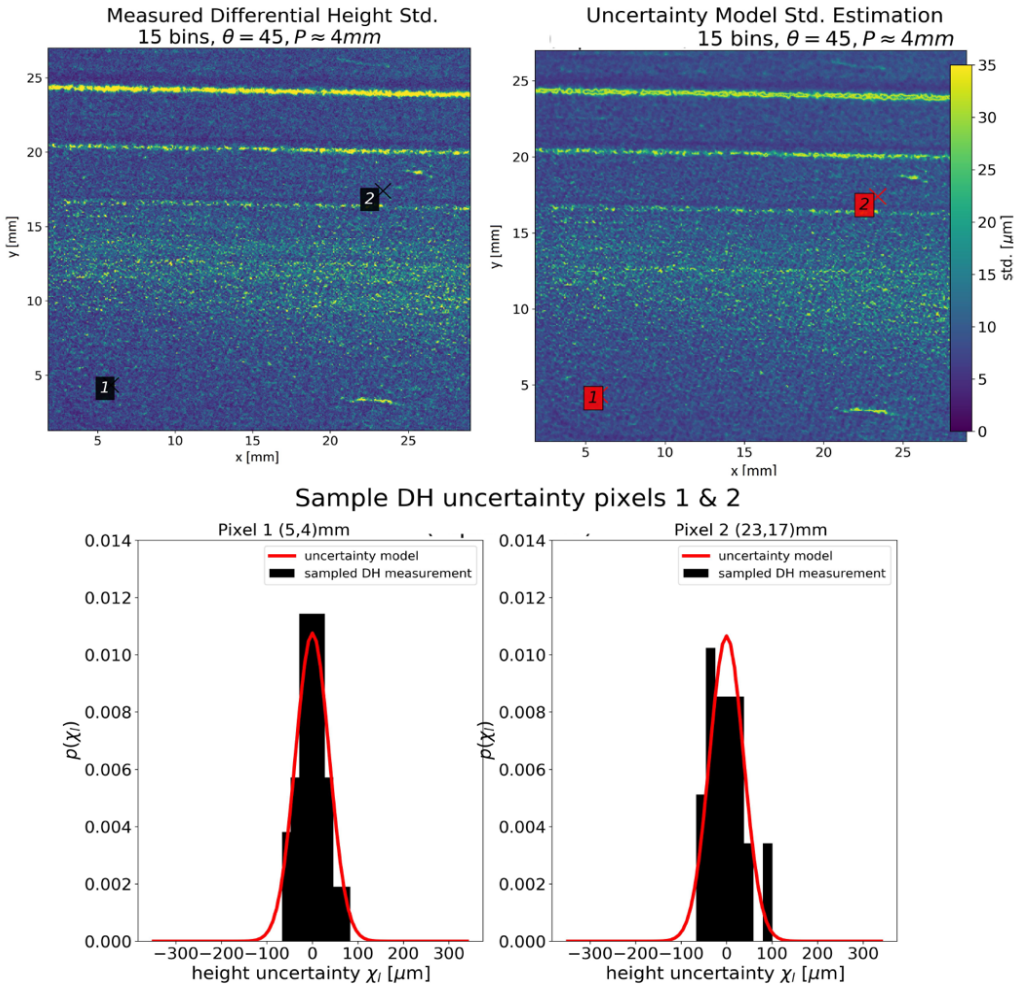

Figure 5. Full field differential height measurement noise of an example "pristine" powder condition; upper left shows measured differential height noise across iterations, upper right shows estimated differential height uncertainty made by the single point uncertainty model, and the lower shows estimated PDFs for local sample pixels 1 and 2 from the two upper sub-figures.

4 CONCLUSION

This work summarized a rigorously-derived measurement model of a digital fringe projection technique, showing how measured pixel intensity noise propagates into surface

height estimation error. The model was verified against simulation and physical experiment with excellent agreement. The system described herein represents a prototype low-cost digital fringe monitoring system that could be used to assist in either decision-supportive part accept/reject criteria or in feedback control of the MAM process.

ACKNOWLEDGEMENTS

This research was funded by Los Alamos National Laboratory (LANL) through the Engineering Institute—a research and education collaboration between LANL and the University of California San Diego's Jacobs School of Engineering. This collaboration promotes multidisciplinary engineering research that develops and integrates advanced predictive modeling, novel sensing systems, and new developments in information technology to address LANL mission relevant problems.

REFERENCES

[1] ASTM. ASTM F2792–10 standard terminology for additive manufacturing technologies.
[2] Kip Hanson. Metal Milestones in 3D Printing. SME (2020) (https://www.sme.org/technologies/articles/2020/march/metal-milestones-in-3d-printing/)
[3] Jamison L Bartlett, Frederick M Heim, Yellapu V Murty, and Xiaodong Li. In situ defect detection in selective laser melting via full-field infrared thermography. *Additive Manufacturing* (2018) **24**:595–605.
[4] Jamison L Bartlett, Alex Jarama, Jonaaron Jones, and Xiaodong Li. Prediction of microstructural defects in additive manufacturing from powder bed quality using digital image correlation. *Materials Science and Engineering: A* (2020) **794**:140002.
[5] Fabio Caltanissetta, Marco Grasso, Stefano Petro, and Bianca Maria Colosimo. Characterization of in-situ measurements based on layerwise imaging in laser powder bed fusion. *Additive Manufacturing* (2018) **24**:183–199.
[6] Zhongwei Li, Xingjian Liu, Shifeng Wen, Piyao He, Kai Zhong, Qingsong Wei, YushengShi, and Sheng Liu. In situ 3D monitoring of geometric signatures in the powder-bed fusion additive manufacturing process via vision sensing methods. *Sensors* (2018) **18**(4):1180.
[7] Yatong An, Jae-Sang Hyun, and Song Zhang. Pixel-wise absolute phase unwrapping using geometric constraints of structured light system. *Optics Express* (2016) **24**(16):18445–18459.
[8] Niall O'Dowd, Adam J. Wachtor, and Michael D. Todd. A model for describing phase-converted image intensity noise in digital fringe projection techniques. *Optics and Lasers in Engineering* (2020) **134**:106293.
[9] Niall O'Dowd, Adam J. Wachor, and Michael D. Todd. A probability density function model describing height estimation uncertainty due to image pixel intensity noise in digital fringe projection measurements. *Optics and Lasers in Engineering* (2021) **138**:106422.
[10] Niall O'Dowd, Adam J. Wachtor, and Michael D. Todd. Effects of Digital Fringe Projection Operational Parameters on Detecting Powder Bed Defects in Additive Manufacturing. *Additive Manufacturing* (2021) **48**:102454.